ACS APPLIED MATERIALS & INTERFACES

Research Article

Cite This: ACS Appl. Mater. Interfaces 2018, 10, 36703−36710

www.acsami.org

Design of Gold Hollow Nanorods with Controllable Aspect Ratio for Multimodal Imaging and Combined Chemo-Photothermal Therapy in the Second Near-Infrared Window

Kai Cai,[†] Weiyun Zhang,[‡] Jin Zhang,[‡] Huiqiao Li,[†] Heyou Han,*[,‡] and Tianyou Zhai*[,†]

[†]State Key Laboratory of Material Processing and Die & Mould Technology, School of Materials Science and Engineering, Huazhong University of Science and Technology (HUST), Wuhan 430074, P. R. China

[‡]State Key Laboratory of Agricultural Microbiology, College of Science, Huazhong Agricultural University (HZAU), Wuhan 430070, P. R. China

Supporting Information

ABSTRACT: Gold nanoparticles (AuNPs) exhibit great potential for biological applications due to their good biocompatibility and tunable localized surface plasmon resonance (LSPR) properties. Currently, although tuning the aspect ratio of a solid structure or designing a hollow structure has been performed to regulate the LSPR properties of AuNPs, the method of preparing hollow anisotropic AuNPs has rarely been reported. In this study, we designed gold hollow nanorods (AuHNRs) with controllable aspect ratios by a Se-doping Te nanorod-templated method with the assistance of L-cysteine. UV−vis−NIR spectra showed that AuHNRs with an aspect ratio of about 3 could have a LSPR peak in the second near-infrared (NIR-II) window, which is only half of the value required by traditional Au nanorods. Moreover, AuHNRs are nontoxic and capable of loading drugs. In vivo experiment revealed that AuHNRs can be used as contrast agents in multimodal imaging, including photothermal imaging, photoacoustic imaging, and computed tomography imaging, as well as in chemo-photothermal combined therapy of tumor in the NIR-II window. Because light in the NIR-II window has remarkable advantages over that in the first near-infrared (NIR-I) window in biomedical applications, AuHNRs can be used as promising NIR-II-window-responsive multifunctional nanoagents.

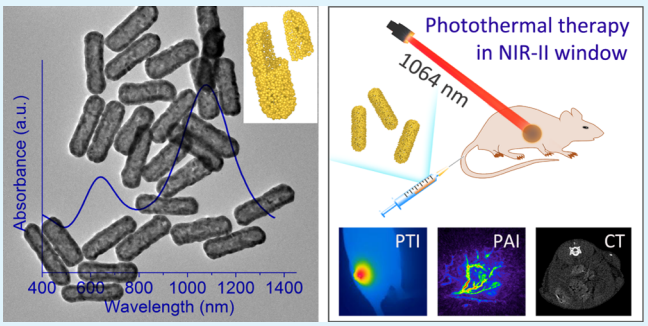

KEYWORDS: *gold hollow nanorods, controllable aspect ratio, NIR-II window, photothermal therapy, multimodal imaging*

INTRODUCTION

Gold nanoparticles (AuNPs) exhibit great potential for biological applications due to their good biocompatibility and tunable localized surface plasmon resonance (LSPR) properties, which are closely related to their size, shape, and structure.[1−3] Up to now, although various types of AuNPs have been reported, only a small number of them can have LSPR peaks in the second near-infrared (NIR-II) window (1000−1350 nm), while most types have LSPR peaks in the first near-infrared (NIR-I) window (700−950 nm).[4−7] It has been demonstrated that light in the NIR-II window is more suitable for biological applications because of its deeper tissue penetration ability, a higher maximum permissible exposure (MPE) value, lower autofluorescence background, and reduced photon scattering.[8−11] However, compared with the studies of the application of NIR-I-window-responsive AuNPs in imaging or antitumor in vivo, those of NIR-II-window-responsive nanoagents are largely inadequate.[12−21] One of the main reasons is the lack of nanoagents that can work in the NIR-II window.[7] Therefore, it is highly desirable to develop new-style available NIR-II-window-responsive AuNPs.

To tune the LSPR peaks into the NIR-II window, a well-known method is to employ Au nanorods (AuNRs) and increase their aspect ratio.[22] However, traditional AuNRs have rarely been used as NIR-II-window-responsive nanoagents in previous reports.[12] Recently, ultrathin or mini AuNRs with tunable plasmonic peaks in the NIR-II window were prepared,[23,24] which may be promising candidates for biological applications due to their advantages in size.[25] Nanostructures with size larger than 200 nm are not suitable for in vivo applications.[26] In addition, modification agents required for controlling the anisotropic growth of AuNRs may cause certain toxicity and their biocompatibility usually needs to be further improved.[27] Another effective method for tuning the red shift of the LSPR peaks is to prepare hollow AuNPs and increase the ratio of the outer diameter to shell thickness.[28,29] Several research groups have made great progress in the study of hollow AuNPs.[30−34] For example,

Received: July 27, 2018
Accepted: October 4, 2018
Published: October 4, 2018

DOI: 10.1021/acsami.8b12758
ACS Appl. Mater. Interfaces 2018, 10, 36703−36710

Xia and co-authors initially developed a template method for preparing Au nanocages and tuning their LSPR peaks into the NIR-II window;[6,30] and by using Co-based nanoparticles as templates, Zhang's group prepared hollow Au nanospheres with LSPR peaks in the NIR-I window.[33,34] Currently, although preparing the hollow structure or tuning the aspect ratio of the solid structure has been carried out to regulate the LSPR properties of AuNPs, the method of preparing hollow anisotropic AuNPs has rarely been reported.

Herein, for the first time, we prepared gold hollow nanorods (AuHNRs) with controllable aspect ratios by a Se-doping Te nanorod-templated method. The modification agent with sulfhydryl played a vital role in shaping the hollow structure in the synthesis. The ultraviolet−visible−NIR (UV−vis−NIR) spectra showed that AuHNRs with an aspect ratio of about 3 could have a LSPR peak in the NIR-II window, which is only half of the value required by solid AuNRs. The results of the in vitro experiments demonstrated that the as-prepared AuHNRs are nontoxic nanoagents and can be used simultaneously as drug carriers and heat generators in the NIR-II window for chemo-photothermal combined therapy. The in vivo experiments revealed that AuHNRs can be used as contrast agents for multimodal imaging, including photothermal imaging, photoacoustic imaging, and computed tomography (CT) imaging, and as a bifunctional platform for chemo-photothermal combined tumor therapy. This study provides a facile method for preparing new-style AuHNRs with controllable aspect ratios and demonstrates that the hollow anisotropic AuNPs possess great potential to be used as NIR-II-window-responsive nanoagents in biological applications.

EXPERIMENTAL SECTION

Materials. Tellurium dioxide powder (TeO_2, 99.99%), selenous acid (H_2SeO_3, 99.99%), 4-nitrophenol (99%), and 4-nitrothiophenol (90%) were purchased from Aladdin Chemistry Co., Ltd. Hydrazine monohydrate (85%, AR), sodium dodecyl sulfate (SDS, 99%), tetrachloroauric(III) acid hydrate ($HAuCl_4$, AR), L-cysteine (Cys, 99%), and glycine (Gly, 99.5%) were provided by Sinopharm Chemical Reagent Co., Ltd. Penicillin−streptomycin, fetal bovine serum (FBS), and Dulbecco's modified Eagle's medium (DMEM) were supplied by GIBCO Invitrogen Corp. Sulfhydryl−poly(ethylene glycol)$_{2000}$ (sulfhydryl−PEG) and doxorubicin hydrochloride (Dox) were provided by Peng Sheng Bio. Corp. (Shanghai, China) and Meilun Biotech Co., Ltd. (Dalian, China), respectively. Thiazolyl blue tetrazolium bromide (MTT) dye was purchased from Sigma-Aldrich. The water used in all experiments was ultrapure (18.2 MΩ). All chemicals were used as received without further purification.

Preparation of AuHNRs. Te nanorods were synthesized by co-reducing Te and Se precursors with hydrazine monohydrate. In a typical synthesis of Te nanorods, tellurium dioxide (16.0 mg), seleninic acid (0.6 mL, 5.43 mM), and hydrazine monohydrate (8 mL) were successively added into a beaker with constant magnetic stirring at 40 °C. After 20 min, the mixture was 10-fold diluted with SDS solution (10 mM) for terminating the reaction and stabilizing Te nanorods. After 10 min of stirring, the mixture was cleaned by repeated centrifugation (10 000 rpm, three times). For the preparation of Te nanorods with different aspect ratios, the amount of seleninic acid was adjusted from 0.6 to V mL (V = 0.1, 0.2, 0.3, 0.4, 0.5, 0.7, 0.8, or 1.0) in the reaction. The obtained Te nanorods were used as templates in the following preparation of AuHNRs. In a typical synthesis, Te nanorods (~0.015 mmol) from the previous experiment were dispersed in L-cysteine solution (90 mL, 2.0 μM) at 5 °C and then $HAuCl_4$ (2.0 mL, 10 mM) was added to the solution under constant magnetic stirring. After 10 min, the mixture was washed by centrifugation (7000 rpm, three times).

In Vivo Antitumor Study. SCC-7 tumor-bearing nude mice were randomly divided into five groups (four mice in each group). Mice were intravenously injected with solutions of phosphate-buffered saline (PBS), AuHNRs (1.0 mg mL^{-1}), or AuHNRs−Dox (1.0 mg mL^{-1}, 6%) every other day. The Se precursor (0.3 mL) was used in the template synthesis of AuHNRs. Four hours after the injection of nanoagents, light treatments (0 or 10 min irradiation, 1064 nm, 400 mW cm^{-2}) were carried out on the mice. The measurement of the tumor size and weight of the mice was conducted before injection with the following equations: V_{tumor} = [(tumor length) × (tumor width)^2]/2, $V_{relative} = V_n/V_1$, and $M_{relative} = M_n/M_1$. On the 18th day, the mice were sacrificed and the heart, liver, spleen, lung, and kidney were collected for histological study via haemotoxylin and eosin (H&E) staining.

In Vivo Multimodal Imaging. For photothermal imaging, mice were injected with PBS (100 μL) or AuHNRs (100 μL, 1.0 mg mL^{-1}). Four hours later, the mice received laser irradiation (1064 nm, 400 mW cm^{-2}) at the preset time, and the photothermal image was collected by an infrared camera (FLIR T250). For computed tomography (CT) imaging, PBS or AuHNRs (100 μL, 1.0 mg mL^{-1}) were first injected, and the CT image was collected at the 4th h after injection. The CT imaging was carried out at Tongji Medical College (HUST). The Se precursor (0.3 mL) was used in the template synthesis of the AuHNRs. For photoacoustic imaging, photoacoustic signals were detected by a small animal photoacoustic imaging system (Endra NEXUS 128, Endra Life Sciences) before and after the injection of AuHNRs (100 μL, 1.0 mg mL^{-1}). The Se precursor (1.0 mL) was used in the template synthesis of the AuHNRs. All the solutions mentioned above for in vivo imaging were injected intravenously through the tail vein.

Material Characterization. Transmission electron microscopy (TEM) imaging was conducted using a FEI TECNAI F30 microscope operated at 200 kV and copper grids were used to load the samples. All values of the material sizes were measured through TEM images. Scanning TEM (STEM) and line-scan energy-dispersive X-ray spectroscopy (EDS) were carried out under the high-angle annular dark field (HAADF) mode with an energy dispersive X-ray analysis attachment. Inductively coupled plasma-mass spectrometry (ICP-MS) measurements were performed using NexION 300Q (PerkinElmer). X-ray diffraction (XRD) was tested on a Bruker D8 Advance X-ray diffractometer with Cu Kα radiation. The samples were prepared by depositing nanostructures on glass. The scanning speed was set as 8° min^{-1}. X-ray photoelectron spectra (XPS) were collected on an ESCALAB 250Xi spectrophotometer (Thermo Fisher) with Al Kα X-ray radiation and calibrated using the C 1s peak (284.6 eV). UV−vis−NIR absorption spectra were measured by a Lambda 750 UV−vis−NIR spectrophotometer (PerkinElmer).

Dox Loading and Releasing. AuHNRs were first modified with sulfhydryl−PEG. In brief, AuHNRs were dispersed in water at a concentration of 5 mg mL^{-1}, and then 200 μL solution mentioned above was added to 9.8 mL water containing 10 mg sulfhydryl−PEG. After gentle stirring for 4 h, the resulting solution was centrifuged (8000 rpm, 5 min) and re-dispersed in water to remove excess PEG. As for drug loading, AuHNRs and Dox were mixed at various ratios for 24 h. The resulting solution was centrifuged and the supernatant was collected to determine the Dox loading efficiency. The Dox loading efficiency was defined as follows: Loading efficiency (%) = $(m_0 - m_1)/m_0 \times 100\%$, in which m_0 is the mass of total Dox and m_1 is the mass of Dox in the supernatant. To study the Dox releasing from the AuHNRs−Dox system, 1.0 mL of AuHNRs−Dox (1 mg mL^{-1}, 6%) was dialyzed against 8 mL phosphate buffer (0.02 mol L^{-1}, pH 6.8 or 7.4). The dialysate was replaced and collected. Dox concentration was detected at a preset time by fluorescence spectrum.

Cytotoxicity in Vitro. The SCC-7 cells were incubated according to the previously reported method.[35] The cytotoxicity of the samples was measured by MTT assay. The biocompatibility of AuHNRs was first studied. DMEM with different concentrations of AuHNR nanoagents and 10% FBS was used in the culture. The SCC-7 cells were seeded in 96-well plates and AuHNR nanoagents were used to replace the culture medium after 24 h. After 12 or 24 h, the medium

DOI: 10.1021/acsami.8b12758
ACS Appl. Mater. Interfaces 2018, 10, 36703−36710

containing AuHNRs was replaced by 200 μL of DMEM, and 20 μL of MTT was added thereafter. After 4 h of culturing, the medium was replaced by dimethyl sulfoxide (DMSO) (150 μL). To examine the antitumor efficiency of combined photothermal therapy and chemotherapy, after the cells were seeded for 24 h, the culture medium containing AuHNRs or AuHNRs−Dox at various concentrations was used to replace the previous medium. Four hours later, fresh medium was used to replace the previous medium again and the wells were treated with or without the 1064 nm laser (200 mW cm^{-2}, 5 min). 24 h later, 200 μL of DMEM was used to replace the medium, and then 20 μL of MTT was added. After 4 h of culturing, the medium was replaced by DMSO (150 μL). The relative cell viability was measured according to the optical density at 570 nm, which was obtained by a microplate reader (Bio-Rad, Model 550).[35] AuHNRs obtained by using 0.3 mL of Se precursor in template preparation were used in the test.

Tumor-Bearing Nude Mice Model. The experiment was conducted on the basis of the guidelines for laboratory animals (HZAU). Babl/C nude mice were supplied by Beijing Huafukang Bioscience Co. Inc. The SCC-7 cells (100 μL, 5 × 10^6 cells) were subcutaneously injected to the right back of mice. After 4 weeks, the tumors reached an approximate size of 100 mm^3.

RESULTS AND DISCUSSION

In the synthesis of Te nanorods, a small quantity of Se precursor was used to regulate their aspect ratios. In a typical synthesis, the amount of Te precursor was 0.10 mmol (0.016 g) while that of the Se precursor was only 3.26 μmol (0.6 mL). TEM images (Figures 1a and S1) of the as-prepared Te nanorods show that these nanoparticles are of rod shape and highly uniform size. EDS analysis (Figure S2) shows that element Te is dominant and Se is rarely present. A high-resolution TEM (HRTEM) image (Figure 1b) of a single nanorod indicates that it is of a single crystal structure and grows along the (001) direction. The *d*-spacing of the adjacent fringes is about 0.58 nm, which corresponds to the (001) lattice planes of a trigonal tellurium (t-Te) crystal.

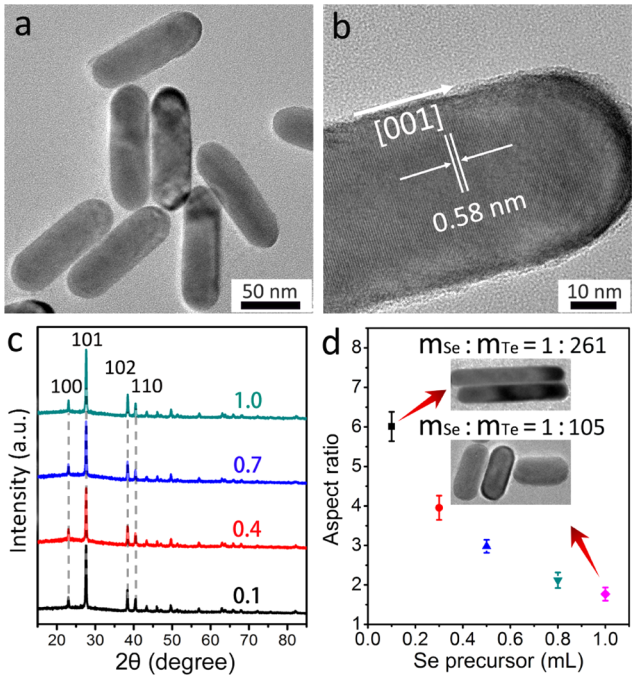

Figure 1. (a) TEM image of Te nanorods. (b) HRTEM image of a Te nanorod. (c) XRD of four Te nanorods obtained by using 0.1, 0.4, 0.7, and 1.0 mL Se precursor (5.43 mM) in synthesis. (d) A statistical illustration of the aspect ratios of Te nanorods obtained with different volumes of Se precursor (5.43 mM) in the synthesis. Insets are TEM images and elemental mass ratios of the corresponding Te nanorods.

By changing the dosage of the Se precursor in the synthesis, the aspect ratio of nanorods could be adjusted. When the dosage of the Se precursor was decreased from 0.6 to 0.1 mL, the nanorods became longer and thinner. As shown in Figure S3a, the average length and diameter turned to about 180 and 30 nm, respectively. Inversely, the nanorods became shorter and thicker with the increasing dosage of the Se precursor in the synthesis (Figure S3b). HRTEM images (Figure S3c,d) show that they also grow along the (001) direction, and their *d*-spacing of adjacent fringes is about 0.58 nm, which is the same as that of nanorods obtained using 0.6 mL of Se precursor. XRD was further used to characterize the crystal structure of Te nanorods. The same results were obtained in spectrograms for four nanorods with different aspect ratios (Figure 1c), and all peaks could be readily indexed to crystalline t-Te (JCPDS 36-1452). These results demonstrate that a small quantity of the Se precursor used in the synthesis does not impact the crystalline structure of Te nanorods. The relationship between the aspect ratio of Te nanorods and the dosage of the Se precursor is illustrated in Figure 1d. ICP-MS was used to analyze the mass ratio of Te to Se. The results show that the ratio was 261:1 and 105:1 when 0.1 and 1.0 mL Se precursor were used, respectively, further demonstrating that the nanorods are Te nanostructures.

Elemental Se and Te belong to the same group in the periodic table and have some similar characteristics. However, Te crystals have a tendency to form one-dimensional structures because the crystal structure of tellurium is highly anisotropic and the crystals always grow along one particular direction,[36] but Se has several allotropic forms, including amorphous Se (a-Se).[37] Under specific reaction conditions, spherical Se colloid could be obtained.[38] In this study, the anisotropic growth of Te crystals could be regulated by the addition of a certain amount of Se precursor, which facilitated the tunable synthesis of Te nanorods. The colors of the solutions containing different Te nanorods showed obvious differences with the variation of the aspect ratio (Figure S4). Figure S5 shows the UV−vis−NIR absorption spectra of six different nanorods obtained by using various amounts of Se precursor in the synthesis. With the increasing amount of Se precursor, the spectra exhibited regular changes, including a red shift of transverse bands and a blue shift of longitudinal bands, indicating the increase in diameter and the decrease in length, respectively.[39]

In the synthesis of AuHNRs, Te nanorods served as a chemical template, $HAuCl_4$ was used as the Au precursor, and L-cysteine was used as the modification agent. Due to the presence of the electrochemical driving force between template elements and Au precursors, the replacement reaction takes place as the following equations: $AuCl_4^- + Te(Se) + H_2O \rightarrow Au + TeO_3^{2-}(SeO_3^{2-}) + Cl^- + H^+$. The fact that all template elements could be oxidized into ions in the reaction is very beneficial to the acquisition of AuNPs with a low residual template components. Figure 2a shows the TEM image of a typical sample of AuHNRs, which shows a rod-shaped outline and a hollow interior. Compared with that of Te templates (Figure S6), the size of AuHNRs was not obviously changed. The typical color of AuHNR solution is blue (inset in Figure 2a). The HRTEM image (Figure 2b) shows that the wall thickness of AuHNRs is about 7.2 nm. Lattice fringes with an

DOI: 10.1021/acsami.8b12758
ACS Appl. Mater. Interfaces 2018, 10, 36703−36710

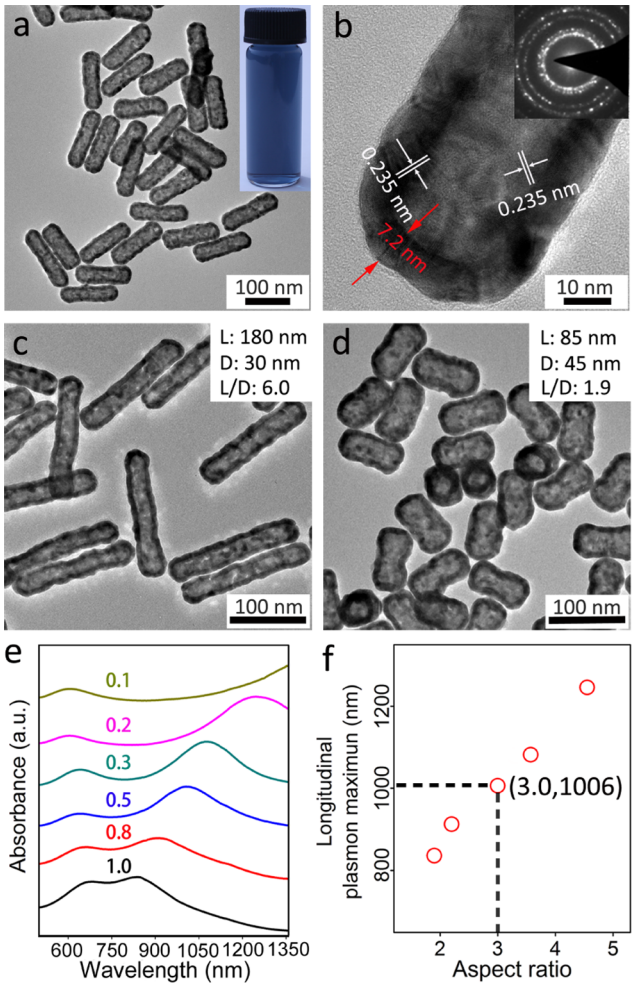

Figure 2. (a) TEM image of AuHNRs. The volume of the Se precursor (5.43 mM) was 0.3 mL in template synthesis. The inset is the photograph of AuHNR solution. (b) The HRTEM image of AuHNRs and the inset is the electron diffraction pattern of AuHNRs. (c, d) TEM images of AuHNRs. The volume of the Se precursor (5.43 mM) was 0.1 and 1.0 mL in the synthesis of corresponding templates. (e) UV−vis−NIR spectra of AuHNRs. The volume of the Se precursor (5.43 mM) was 0.1, 0.2, 0.3, 0.5, 0.8, and 1.0 mL in the synthesis of corresponding templates. (f) Longitudinal plasmon maximum of AuHNRs with different aspect ratios.

interplanar spacing of 0.235 nm were repeatedly observed in the structure, which corresponds to the (111) lattice plane of face-centered cubic (fcc) Au. The electron diffraction pattern (inset in Figure 2b) confirms that the AuHNRs are polycrystalline structures. Due to the effect of the galvanic replacement reaction and the Kirkendall effect, some pinholes are formed among crystalline grains and are present in the shell.[40] A HAADF-STEM image (Figure S7) clearly shows that the nanorods are of hollow structure, which is also supported by the cross-sectional line profiles. EDS analysis (Figure S8) shows that the structure is composed of Au element. ICP-MS analysis reveals the presence of 5.6% Te in the as-prepared AuHNRs. The structure was further tested by XRD. As shown in Figure S9, all peaks can be assigned to a fcc phase of Au (JCPDS 65-2870). The XPS analysis (Figure S10) shows that the main component is element Au. The high-resolution Au 4f spectrum displays two peaks at binding energies of 87.28 and 83.68 eV, which correspond to Au $4f_{5/2}$ and Au $4f_{7/2}$, respectively.

By choosing different templates in synthesis, AuHNRs with different aspect ratios could be obtained. TEM images (Figures 2c,d and S11) show that AuHNRs with aspect ratios from 6.0 to 1.9 were obtained, all of which were of obvious hollow structures. Although the change in the aspect ratio is evident, the variation of the shell thickness is not remarkable. As shown by the HRTEM images (Figure S12), the shell thickness only became slightly thinner at larger aspect ratios when different templates were used. UV−vis−NIR absorption spectra of a series of AuHNRs (Figure 2e) show that a wide shift occurred in their LSPR peaks and the AuHNRs exhibited a variation tendency in the band shift similar to that of the template. The increase in diameter led to a red shift of the transverse plasmon bands, and simultaneously the decrease in length resulted in a blue shift of the longitudinal plasmon bands. The statistical information of the longitudinal plasmon maximum of AuHNRs with different aspect ratios is listed in Figure 2f. TEM images of the five samples are shown in Figures 2a,d, S11, and S13. It is noteworthy that AuHNRs with the aspect ratio of 3.0 (diameter = 38 nm, length = 115 nm) have a longitudinal plasmon peak at 1006 nm. In contrast, the aspect ratio of traditional AuNRs needs to be increased to approximately 6 when adjusting the LSPR peak red shift in the NIR-II window.[6] Similar to the case of AuNRs, the increase in the aspect ratio of AuHNRs can lead to a red shift of their longitudinal LSPR peaks. However, compared with AuNRs, AuHNRs exhibited a larger red shift at the same variation in the aspect ratio due to the cavity and thinner shell. Besides, compared with the hollow Au nanospheres, the red shift of the LSPR peaks is more likely to occur in AuHNRs because of the anisotropic structure.

In the synthesis, regular AuHNRs could be obtained only in a narrow range of L-cysteine concentrations. When the concentration was increased from 2 to 8 μM, many tiny nanograins would appear on the surface of the product; and when the concentration was decreased to 0.4 μM, the product would be of a broken structure with big holes (Figure S14). We speculate that the sulfhydryl (−SH) of L-cysteine (Cys) plays an important role in the process. To confirm this speculation, instead of using L-cysteine, we used another amino acid, glycine (Gly). Compared with L-cysteine, glycine also possesses amidogen ($-NH_2$) and carboxyl (−COOH) but lacks sulfhydryl (−SH) (Figure 3a). When glycine was used at the same concentration in the synthesis, only broken structures could be obtained (Figure 3b). To further verify the effect of sulfhydryl, a controlled experiment was conducted, in which 4-nitrothiophenol (4-NTP) and 4-nitrophenol (4-NP) were used as the modification agents respectively (Figure 3a). As expected, well-formed structures could be obtained only when 4-nitrothiophenol was used in the synthesis (Figure 3c,d). Because sulfhydryl can form a relatively strong Au−thiol bond (184 kJ mol^{-1}), sulfhydryl might greatly affect the reaction dynamics of the galvanic replacement reaction. Moreover, Au−thiol bonds on the surface may weaken the Ostwald ripening of Au nanoparticles, which is conducive to the maintenance of the initial morphology. Hence, using molecules containing sulfhydryl can contribute to the generation of well-formed hollow nanorods.

Prior to the biological applications, the photothermal properties of the as-prepared AuHNRs were studied first. The UV−vis−NIR absorption spectra of the sample (in Figure 2a) and the measured results are listed in Figure 4a,b,

DOI: 10.1021/acsami.8b12758
ACS Appl. Mater. Interfaces 2018, 10, 36703−36710

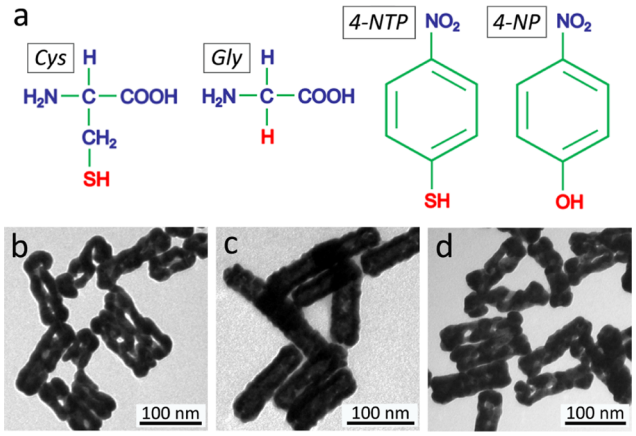

Figure 3. (a) Chemical structural formulas of L-cysteine (Cys), glycine (Gly), 4-nitrothiophenol (4-NTP), and 4-nitrophenol (4-NP). (b–d) TEM images of Au nanostructures obtained by using Gly (b), 4-NTP (c), and 4-NP (d) as the modification agents at the same concentration as Cys (2 μM) in the synthesis.

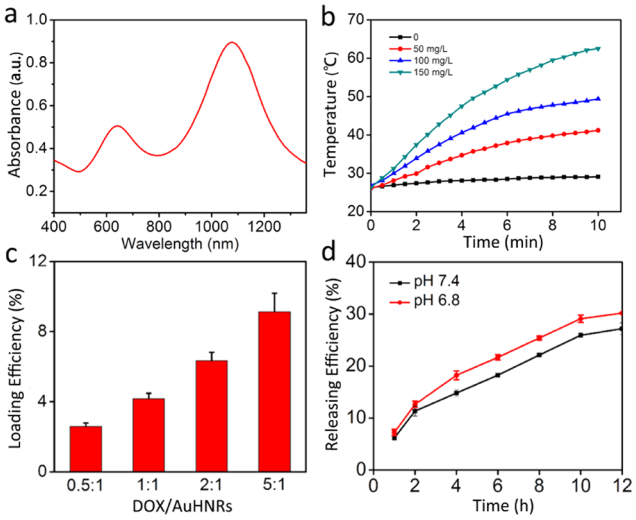

Figure 4. (a) UV–vis–NIR spectrum of AuHNRs (in Figure 2a). The sample was obtained using 0.3 mL Se precursor (5.43 mM) in the template synthesis. (b) Temperature changes of different AuHNRs suspensions under 1064 nm laser irradiation. The volume of each solution was 2.0 mL and the laser power was 690 mW. (c) Dox loading efficiency of AuHNRs. (d) Dox releasing efficiency of AuHNRs.

respectively. In the test, the laser wavelength was 1064 nm. The temperature of the solution containing 0.15 mg mL^{-1} AuHNRs was increased by more than 35 °C in 10 min. In contrast, no obvious increase was observed in the blank control group. Further experiment showed that the photothermal conversion efficiency of AuHNRs was 33% (Figure S15). We then studied the drug loading and releasing efficiency of the AuHNRs. Before loading with drug molecules, AuHNRs were modified with PEG to improve the colloidal stability. The results (Figure 4c,d) show that the loading efficiency can be improved by increasing the drug concentration and the drug can be gradually released from AuHNRs in PBS solution. Besides loading on the surface of AuHNRs, drugs could also be loaded in the cavities because of the hollow porous structure.[32]

In addition, the biocompatibility of the as-prepared AuHNRs was tested in vitro in two different incubation times. As shown in Figure 5a, at a concentration as high as 2.0 mg mL^{-1}, the cell viability was above 98.3% after 12 or 24 h of

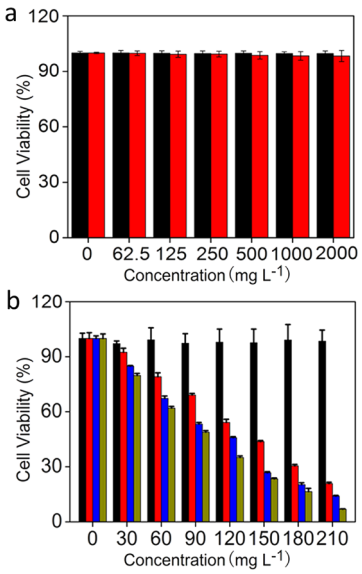

Figure 5. (a) Cell viability of bare AuHNRs (in Figure 2a) with different co-culture times. Black: 12 h. Red: 24 h. (b) In vitro antitumor efficiency against SCC-7 cells. Black: PBS. Red: AuHNRs–Dox. Blue: AuHNRs + 1064 nm laser irradiation. Brown: AuHNRs–Dox + 1064 nm laser irradiation.

incubation with AuHNRs, demonstrating the excellent biological compatibility of AuHNRs. It is noteworthy that the AuHNRs were used in the test after centrifugal cleaning following the galvanic replacement reaction. There may be two important reasons contributing to the nontoxicity of AuHNRs: element Au has high chemical/biological inertness and the modification agent is absolutely nontoxic. On account of the intrinsic capacity of drug loading and photothermal conversion of AuHNRs, they could be used as ideal nanoagents for combined cancer therapy. We then studied the antitumor efficiency of AuHNRs through MTT assay. The results (Figure 5b) indicate remarkable efficiency of AuHNRs in either 1064 nm laser irradiation or drug loading. Particularly, the highest efficiency could be achieved when laser irradiation and drug loading were combined.

In the in vivo application, the photothermal imaging was performed first. The laser wavelength used in the experiment was also 1064 nm. As shown in Figure 6a, the tumor temperature increased rapidly in the experiment group while did not show obvious changes in the control group. Because the photothermal effect of AuHNRs can cause ultrasound signals, photoacoustic imaging could also be conducted with AuHNRs. As the excitation wavelength in the equipment is limited in the NIR-I window, we chose usual 808 nm laser for the test with AuHNRs in Figure 2d. The results of photoacoustic imaging (Figure 6b) show that after injection of AuHNRs, the photoacoustic signal became increasingly clear over time, indicating that the concentration of AuHNRs in the tumor increased over time. Because of the enhanced permeability and retention effect of cancerous tumors, AuHNRs could permeate into the tumor tissue along vessels and accumulate in the tumor area.[41] In this study, the moderate size and the nontoxic feature of AuHNRs probably contribute to a prolonged blood circulation, which can lead to

DOI: 10.1021/acsami.8b12758
ACS Appl. Mater. Interfaces 2018, 10, 36703–36710

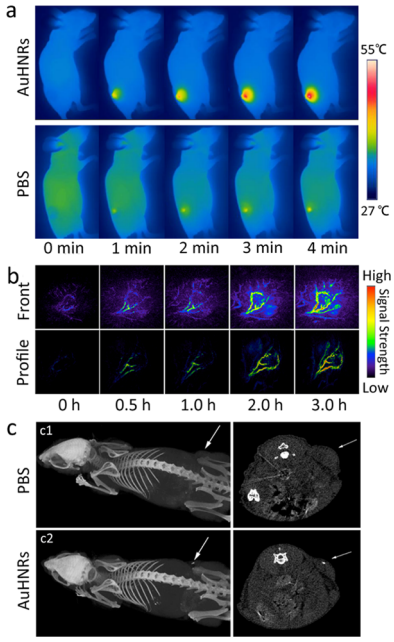

Figure 6. (a) Photothermal images (PTI) of mice at the 4th h post-injection of AuHNRs (in Figure 2a) under 1064 nm laser irradiation at different time points. (b) Photoacoustic images from the front view and profile view at different time points. The wavelength of laser was 808 nm and the used AuHNRs were obtained using 1.0 mL Se precursor (5.43 mM) in the template synthesis (in Figure 2d). (c) Three-dimensional reconstructed CT images of mice with injection of PBS (c1) and AuHNRs (c2). Arrows point to the tumor site.

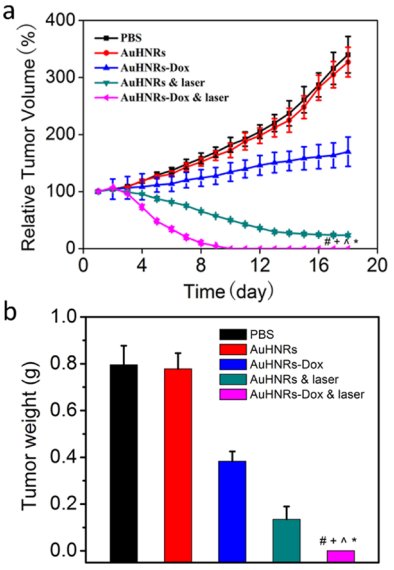

Figure 7. (a) Relative tumor volume during in vivo antitumor treatment. (b) Average tumor weight on the 18th day. #$p < 0.01$, +$p < 0.01$, ∧$p < 0.01$, and *$p < 0.01$ were tested via a Student's t test when the group was compared with groups treated with PBS, AuHNRs, AuHNRs−Dox, and AuHNRs + irradiation (10 min), respectively.

a high accumulation of AuHNRs in the tumor. In addition, because Au is a high-Z element with strong X-ray attenuation ability,[42] AuHNRs could be used as CT imaging contrast agents. As shown in Figure 6c, three-dimensional reconstructed CT images reveal that the tumor area is bright in the mouse with the injection of AuHNRs, indicating that AuHNRs can be used as CT imaging contrast agents. Taken together, the above results demonstrate that AuHNRs have the potential to be used as multifunctional contrast agents for imaging.

We then further investigated the antitumor effect of AuHNRs in vivo. It is noteworthy that the laser power used in the process was 0.4 W cm^{-2}, which is much lower than the MPE value.[8] As shown in Figure 7, through a combination therapy involving photothermal therapy and chemotherapy, the xenograft tumor completely disappeared after 10 days. In contrast, a single therapy did not exhibit such an obvious therapeutic effect, especially the single chemotherapy, which can hardly inhibit the growth of the tumor. Heating can not only facilitate the release of drug, but also kill cancer cells immediately. Therefore, the combined therapy exhibits a remarkably better curative effect than single therapies. During the treatment, the weight of the mice was not obviously changed (Figure S16) and no deterioration was observed in the main organs (Figure S17). These results imply that AuHNRs can be used as nanoagents in chemo-photothermal tumor therapy without causing side effects during the treatment.

CONCLUSIONS

We prepared hollow anisotropic AuNPs with controllable aspect ratios by a Se-doping Te nanorod-templated method with the assistance of L-cysteine. AuHNRs not only have the advantage of nontoxicity, but also show outstanding properties for biomedical applications. In this study, we demonstrated that AuHNRs can be used as multifunctional contrast agents for multimodal imaging. Moreover, AuHNRs exhibit a good curative effect in chemo-photothermal combined therapy of tumor when used to load drugs under 1064 nm laser irradiation. Because AuHNRs with an aspect ratio as low as 3 can have LSPR peaks in the NIR-II window, they can also be used as NIR-II-window-responsive nanoagents of small size for photothermal imaging, photoacoustic imaging and photothermal therapy. Finally, due to their hollow structure, AuHNRs could be used to load drugs for targeted transport. In summary, the novel AuHNRs can be a promising multifunctional platform for the diagnosis and treatment of cancer.

ASSOCIATED CONTENT

Supporting Information

The Supporting Information is available free of charge on the ACS Publications website at DOI: 10.1021/acsami.8b12758.

TEM images, HRTEM images, HAADF-STEM image, line-scan EDS spectrum, photograph, UV−vis−NIR spectrum, EDS, XRD, XPS of Te nanorods or AuHNRs, relative body weights of mice during the treatment, H&E stained images (PDF)

AUTHOR INFORMATION

Corresponding Authors

*E-mail: hyhan@mail.hzau.edu.cn (H.H.).
*E-mail: zhaity@hust.edu.cn (T.Z.).

ORCID

Huiqiao Li: 0000-0001-8114-2542
Heyou Han: 0000-0001-9406-0722
Tianyou Zhai: 0000-0003-0985-4806

DOI: 10.1021/acsami.8b12758
ACS Appl. Mater. Interfaces 2018, 10, 36703−36710

Author Contributions

This manuscript was written through contributions of all authors. All authors have given approval to the final version of the manuscript.

Notes

The authors declare no competing financial interest.

■ ACKNOWLEDGMENTS

We acknowledge the financial support from the National Basic Research Program of China (2015CB932600), the National Natural Science Foundation of China (91622117, 51472097, 51727809, 21778020), the National Key R&D Program (2016YFB0401100, 2016YFD0500700), the China Postdoctoral Science Foundation (2017M622428), and the Fundamental Research Funds for the Central Universities (2015ZDTD038, 2017KFKJXX007).

■ REFERENCES

(1) Kumar, A.; Kim, S.; Nam, J.-M. Plasmonically Engineered Nanoprobes for Biomedical Applications. *J. Am. Chem. Soc.* **2016**, *138*, 14509−14525.

(2) Chen, W.; Zhang, S.; Yu, Y.; Zhang, H.; He, Q. Structural-Engineering Rationales of Gold Nanoparticles for Cancer Theranostics. *Adv. Mater.* **2016**, *28*, 8567−8585.

(3) Cheng, L.; Wang, C.; Feng, L.; Yang, K.; Liu, Z. Functional Nanomaterials for Phototherapies of Cancer. *Chem. Rev.* **2014**, *114*, 10869−10939.

(4) Dreaden, E. C.; Alkilany, A. M.; Huang, X.; Murphy, C. J.; El-Sayed, M. A. The Golden Age: Gold Nanoparticles for Biomedicine. *Chem. Soc. Rev.* **2012**, *41*, 2740−2779.

(5) Abadeer, N. S.; Murphy, C. J. Recent Progress in Cancer Thermal Therapy Using Gold Nanoparticles. *J. Phys. Chem. C* **2016**, *120*, 4691−4716.

(6) Yang, X.; Yang, M.; Pang, B.; Vara, M.; Xia, Y. Gold Nanomaterials at Work in Biomedicine. *Chem. Rev.* **2015**, *115*, 10410−10488.

(7) Park, J.; Kim, M.; Hwang, J.; Nam, J.-M. Golden Opportunities: Plasmonic Gold Nanostructures for Biomedical Applications based on the Second Near-Infrared Window. *Small Methods* **2017**, *1*, No. 1600032.

(8) Jiang, Y.; Upputuri, P. K.; Xie, C.; Lyu, Y.; Zhang, L.; Xiong, Q.; Pramanik, M.; Pu, K. Broadband Absorbing Semiconducting Polymer Nanoparticles for Photoacoustic Imaging in Second Near-Infrared Window. *Nano Lett.* **2017**, *17*, 4964−4969.

(9) Sun, T.; Dou, J.-H.; Liu, S.; Wang, X.; Zheng, X.; Wang, Y.; Pei, J.; Xie, Z. Second Near-Infrared Conjugated Polymer Nanoparticles for Photoacoustic Imaging and Photothermal Therapy. *ACS Appl. Mater. Interfaces* **2018**, *10*, 7919−7926.

(10) Ding, X.; Liow, C. H.; Zhang, M.; Huang, R.; Li, C.; Shen, H.; Liu, M.; Zou, Y.; Gao, N.; Zhang, Z.; Li, Y.; Wang, Q.; Li, S.; Jiang, J. Surface Plasmon Resonance Enhanced Light Absorption and Photothermal Therapy in the Second Near-Infrared Window. *J. Am. Chem. Soc.* **2014**, *136*, 15684−15693.

(11) Smith, A. M.; Mancini, M. C.; Nie, S. Second Window for in vivo Imaging. *Nat. Nanotechnol.* **2009**, *4*, 710−711.

(12) Tsai, M.-F.; Chang, S.-H. G.; Cheng, F.-Y.; Shanmugam, V.; Cheng, Y.-S.; Su, C.-H.; Yeh, C.-S. Au Nanorod Design as Light-Absorber in the First and Second Biological Near-Infrared Windows for in Vivo Photothermal Therapy. *ACS Nano* **2013**, *7*, 5330−5342.

(13) Jiang, Y.; Li, J.; Zhen, X.; Xie, C.; Pu, K. Dual-Peak Absorbing Semiconducting Copolymer Nanoparticles for First and Second Near-Infrared Window Photothermal Therapy: A Comparative Study. *Adv. Mater.* **2018**, *30*, No. 1705980.

(14) Zheng, T.; Li, G. G.; Zhou, F.; Wu, R.; Zhu, J.-J.; Wang, H. Gold-Nanosponge-Based Multistimuli-Responsive Drug Vehicles for Targeted Chemo-Photothermal Therapy. *Adv. Mater.* **2016**, *28*, 8218−8226.

(15) Sun, H.; Su, J.; Meng, Q.; Yin, Q.; Chen, L.; Gu, W.; Zhang, Z.; Yu, H.; Zhang, P.; Wang, S.; Li, Y. Cancer Cell Membrane-Coated Gold Nanocages with Hyperthermia-Triggered Drug Release and Homotypic Target Inhibit Growth and Metastasis of Breast Cancer. *Adv. Funct. Mater.* **2017**, *27*, No. 1604300.

(16) Vijayaraghavan, P.; Liu, C.-H.; Vankayala, R.; Chiang, C.-S.; Hwang, K. C. Designing Multi-Branched Gold Nanoechinus for NIR Light Activated Dual Modal Photodynamic and Photothermal Therapy in the Second Biological Window. *Adv. Mater.* **2014**, *26*, 6689−6695.

(17) Zhou, J.; Jiang, Y.; Hou, S.; Upputuri, P. K.; Wu, D.; Li, J.; Wang, P.; Zhen, X.; Pramanik, M.; Pu, K.; Duan, H. Compact Plasmonic Blackbody for Cancer Theranosis in the Near-Infrared II Window. *ACS Nano* **2018**, *12*, 2643−2651.

(18) Bi, C.; Chen, J.; Chen, Y.; Song, Y.; Li, A.; Li, S.; Mao, Z.; Gao, C.; Wang, D.; Möhwald, H.; Xia, H. Realizing a Record Photothermal Conversion Efficiency of Spiky Gold Nanoparticles in the Second Near-Infrared Window by Structure-Based Rational Design. *Chem. Mater.* **2018**, *30*, 2709−2718.

(19) Li, X.; Zhou, J.; Liu, C.; Xiong, Q.; Duan, H.; Cheung, P. C. K. Stable and Biocompatible Mushroom β-Glucan Modified Gold Nanorods for Cancer Photothermal Therapy. *J. Agric. Food Chem.* **2017**, *65*, 9529−9536.

(20) Dong, Q.; Wang, X.; Hu, X.; Xiao, L.; Zhang, L.; Song, L.; Xu, M.; Zou, Y.; Chen, L.; Chen, Z.; Tan, W. Simultaneous Application of Photothermal Therapy and an Anti-inflammatory Prodrug using Pyrene−Aspirin-Loaded Gold Nanorod Graphitic Nanocapsules. *Angew. Chem., Int. Ed.* **2018**, *57*, 177−181.

(21) Liu, J.; Liang, H.; Li, M.; Luo, Z.; Zhang, J.; Guo, X.; Cai, K. Tumor Acidity Activating Multifunctional Nanoplatform for NIR-mediated Multiple Enhanced Photodynamic and Photothermal Tumor Therapy. *Biomaterials* **2018**, *157*, 107−124.

(22) Li, N.; Zhao, P.; Astruc, D. Anisotropic Gold Nanoparticles: Synthesis, Properties, Applications, and Toxicity. *Angew. Chem., Int. Ed.* **2014**, *53*, 1756−1789.

(23) Chang, H.-H.; Murphy, C. J. Mini Gold Nanorods with Tunable Plasmonic Peaks beyond 1000 nm. *Chem. Mater.* **2018**, *30*, 1427−1435.

(24) Takahata, R.; Yamazoe, S.; Koyasu, K.; Imura, K.; Tsukuda, T. Gold Ultrathin Nanorods with Controlled Aspect Ratios and Surface Modifications: Formation Mechanism and Localized Surface Plasmon Resonance. *J. Am. Chem. Soc.* **2018**, *140*, 6640−6647.

(25) Song, J.; Yang, X.; Jacobson, O.; Huang, P.; Sun, X.; Lin, L.; Yan, X.; Niu, G.; Ma, Q.; Chen, X. Ultrasmall Gold Nanorod Vesicles with Enhanced Tumor Accumulation and Fast Excretion from the Body for Cancer Therapy. *Adv. Mater.* **2015**, *27*, 4910−4917.

(26) Blanco, E.; Shen, H.; Ferrari, M. Principles of Nanoparticle Design for Overcoming Biological Barriers to Drug Delivery. *Nat. Biotechnol.* **2015**, *33*, 941−951.

(27) Zhang, L.; Su, H.; Cai, J.; Cheng, D.; Ma, Y.; Zhang, J.; Zhou, C.; Liu, S.; Shi, H.; Zhang, Y.; Zhang, C. A Multifunctional Platform for Tumor Angiogenesis-Targeted Chemo-Thermal Therapy Using Polydopamine-Coated Gold Nanorods. *ACS Nano* **2016**, *10*, 10404−10417.

(28) Zhang, J. Z. Biomedical Applications of Shape-Controlled Plasmonic Nanostructures: A Case Study of Hollow Gold Nanospheres for Photothermal Ablation Therapy of Cancer. *J. Phys. Chem. Lett.* **2010**, *1*, 686−695.

(29) Genç, A.; Patarroyo, J.; Sancho-Parramon, J.; Bastús, N. G.; Puntes, V.; Arbiol, J. Hollow Metal Nanostructures for Enhanced Plasmonics: Synthesis, Local Plasmonic Properties and Applications. *Nanophotonics* **2017**, *6*, 193−213.

(30) Sun, Y.; Xia, Y. Shape-Controlled Synthesis of Gold and Silver Nanoparticles. *Science* **2002**, *298*, 2176−2179.

(31) Liang, H. P.; Wan, L.; Bai, C.; Jiang, L. Gold Hollow Nanospheres: Tunable Surface Plasmon Resonance Controlled by Interior-Cavity Sizes. *J. Phys. Chem. B* **2005**, *109*, 7795−7800.

DOI: 10.1021/acsami.8b12758
ACS Appl. Mater. Interfaces 2018, 10, 36703−36710

(32) Adams, S.; Zhang, J. Z. Unique Optical Properties and Applications of Hollow Gold Nanospheres (HGNs). *Coord. Chem. Rev.* **2016**, *320*−*321*, 18−37.
(33) Schwartzberg, A. M.; Olson, T. Y.; Talley, C. E.; Zhang, J. Z. Synthesis, Characterization, and Tunable Optical Properties of Hollow Gold Nanospheres. *J. Phys. Chem. B* **2006**, *110*, 19935−19944.
(34) Lindley, S. A.; Cooper, J. K.; Rojas-Andrade, M. D.; Fung, V.; Leahy, C. J.; Chen, S.; Zhang, J. Z. Highly Tunable Hollow Gold Nanospheres: Gaining Size Control and Uniform Galvanic Exchange of Sacrificial Cobalt Boride Scaffolds. *ACS Appl. Mater. Interfaces* **2018**, *10*, 12992−13001.
(35) Han, K.; Zhang, W.-Y.; Zhang, J.; Lei, Q.; Wang, S.-B.; Liu, J.-W.; Zhang, X.-Z.; Han, H.-Y. Acidity-Triggered Tumor-Targeted Chimeric Peptide for Enhanced Intra-Nuclear Photodynamic Therapy. *Adv. Funct. Mater.* **2016**, *26*, 4351−4361.
(36) He, Z.; Yang, Y.; Liu, J.-W.; Yu, S.-H. Emerging Tellurium Nanostructures: Controllable Synthesis and Their Applications. *Chem. Soc. Rev.* **2017**, *46*, 2732−2753.
(37) Mondal, K.; Roy, P.; Srivastava, S. K. Facile Biomolecule-Assisted Hydrothermal Synthesis of Trigonal Selenium Microrods. *Cryst. Growth Des.* **2008**, *8*, 1580−1584.
(38) Jeong, U.; Xia, Y. Synthesis and Crystallization of Monodisperse Spherical Colloids of Amorphous Selenium. *Adv. Mater.* **2005**, *17*, 102−106.
(39) Lin, Z.-H.; Yang, Z.; Chang, H.-T. Preparation of Fluorescent Tellurium Nanowires at Room Temperature. *Cryst. Growth Des.* **2008**, *8*, 351−357.
(40) González, E.; Arbiol, J.; Puntes, V. F. Carving at the Nanoscale: Sequential Galvanic Exchange and Kirkendall Growth at Room Temperature. *Science* **2011**, *334*, 1377−1380.
(41) Maeda, H.; Nakamura, H.; Fang, J. The EPR Effect for Macromolecular Drug Delivery to Solid Tumors: Improvement of Tumor Uptake, Lowering of Systemic Toxicity, and Distinct Tumor Imaging in vivo. *Adv. Drug Delivery Rev.* **2013**, *65*, 71−79.
(42) Goswami, N.; Luo, Z.; Yuan, X.; Leong, D. T.; Xie, J. Engineering Gold-Based Radiosensitizers for Cancer Radiotherapy. *Mater. Horiz.* **2017**, *4*, 817−831.

DOI: 10.1021/acsami.8b12758
ACS Appl. Mater. Interfaces 2018, 10, 36703−36710